High-throughput, label-free, single-cell photoacoustic microscopy of intratumoral metabolic heterogeneity

Pengfei Hai[1,2,7], Toru Imai[1,2,7], Song Xu[3], Ruiying Zhang[1], Rebecca L. Aft[4,5], Jun Zou [3]* and Lihong V. Wang [2,6]*

Intratumoral heterogeneity, which is manifested in almost all of the hallmarks of cancer, including the significantly altered metabolic profiles of cancer cells, represents a challenge to effective cancer therapy. High-throughput measurements of the metabolism of individual cancer cells would allow direct visualization and quantification of intratumoral metabolic heterogeneity, yet the throughputs of current measurement techniques are limited to about 120 cells per hour. Here, we show that single-cell photoacoustic microscopy can reach throughputs of approximately 12,000 cells per hour by trapping single cells with blood in an oxygen-diffusion-limited high-density microwell array and by using photoacoustic imaging to measure the haemoglobin oxygen change (that is, the oxygen consumption rate) in the microwells. We demonstrate the capability of this label-free technique by performing high-throughput single-cell oxygen-consumption-rate measurements of cultured cells and by imaging intratumoral metabolic heterogeneity in specimens from patients with breast cancer. High-throughput single-cell photoacoustic microscopy of oxygen consumption rates should enable the faster characterization of intratumoral metabolic heterogeneity.

Tumours consist of heterogeneous populations of cancer cells that have distinct genetic and phenotypic profiles. The heterogeneity within a tumour, namely intratumoral heterogeneity, has become a great challenge for effective cancer therapy due to the differential response of cells in a tumour[1]. It exists among the hallmarks of cancer, which include acquired cell motility that leads to metastasis, elevated angiogenic potential that leads to angiogenesis and altered cellular metabolism[2]. It is well known that cancer cells have significantly altered metabolic profiles compared with their normal cellular counterparts and many emerging treatment modalities target the cellular metabolism of a tumour[3]. Assessing the extent of intratumoral metabolic heterogeneity would greatly contribute to our understanding of the effect of metabolic heterogeneity on tumour growth, invasion and drug resistance[4]. It will also help design effective and personalized treatment strategies by predicting sensitivity or resistance. Although advances in genome sequencing and RNA analysis have revealed intratumoral metabolic heterogeneity at the genetic level[5], little is known about the heterogeneous metabolic phenotypes.

With greatly improved biomedical imaging tools, the phenotypic landscape of intratumoral metabolic heterogeneity can now be studied directly on bulk populations of cells[6]. Unfortunately, the limitations of the current methodology have prevented such studies on a single-cell level. Metabolic heterogeneity can be imaged and estimated by positron emission tomography in vivo in humans[7]. However, the spatial resolution of positron emission tomography is too poor to make any wider inferences[8]. Fluorescence-based methods have also been used but the required labelling may perturb the original microenvironments of tumour cells[9,10]. Optical imaging techniques based on endogenous contrasts, such as nicotinamide adenine dinucleotide and flavin adenine dinucleotide, can assess the metabolic states of single cells without labelling[11]. However, these techniques cannot provide absolute metabolic measurements, which is not sufficient to study intratumoral metabolic heterogeneity[12,13].

The oxygen consumption rate (OCR) of a cell is directly related to its metabolism[13]. The distribution of the single-cell OCRs within a tumour is an important gauge of metabolic heterogeneity. Extracellular flux analysis with commercially available Seahorse XF Analyzers (Seahorse Bioscience) is the most popular method for high-throughput OCR measurement and has provided valuable insights on the metabolic states of living cells[14]. However, it is performed on bulk populations of cells (~5,000), thus providing little information on cell-to-cell metabolic heterogeneity. To accurately measure single-cell OCRs, each cell must be sealed into a small oxygen-diffusion-limited environment where the temporal change of oxygen content can be monitored. To create such an environment, microwell arrays are usually designed to trap a single cell in each microwell[15]. Single-cell OCR measurements have previously been performed by electrical and fluorescent methods, which require microscale oxygen sensors to monitor the change in oxygen content[16,17]. To perform single-cell OCR measurements on a large population of cells with these methods requires embedding a massive array of microscale oxygen sensors into the microwell array, making it extremely challenging to fabricate and use. Moreover, the embedded microscale oxygen sensors may adversely affect the normal metabolism of cells, rendering the OCR measurement

[1]Department of Biomedical Engineering, Washington University in St. Louis, St. Louis, MO, USA. [2]Caltech Optical Imaging Laboratory, Andrew and Peggy Cherng Department of Medical Engineering, California Institute of Technology, Pasadena, CA, USA. [3]Department of Electrical and Computer Engineering, Texas A&M University, College Station, TX, USA. [4]Department of Surgery, School of Medicine, Washington University, St. Louis, MO, USA. [5]John Cochran Veterans Hospital, St. Louis, MO, USA. [6]Caltech Optical Imaging Laboratory, Department of Electrical Engineering, California Institute of Technology, Pasadena, CA, USA. [7]These authors contributed equally: Pengfei Hai, Toru Imai. *e-mail: junzou@ece.tamu.edu; LVW@caltech.edu
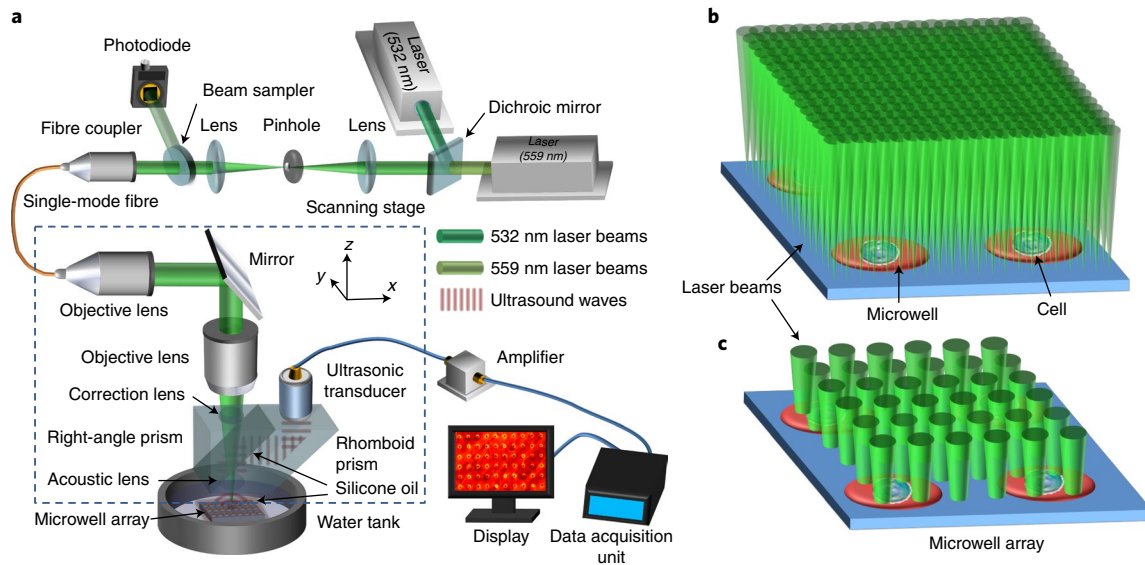
Fig. 1 | System schematic and working modes of SCM-PAM. a, System schematic of SCM-PAM. **b**, High-resolution mode of SCM-PAM with optical-diffraction-limited lateral resolution. **c**, High-throughput mode of SCM-PAM with a single-cell metabolism measurement throughput of about 3,000 cells over 15 min.

inaccurate. Absorption spectroscopy with widely available plate readers may also be used. However, the strong scattering of the cells and the large volume of microwells in plates prevent it from accurately measuring the single-cell OCR. Limited by these issues, single-cell OCR measurement has been accomplished with a capability of only about 30 cells[18]. However, to obtain statistically sound data and assess the entire spectrum of intratumoral metabolic heterogeneity, single-cell OCRs of a large number of cells need to be measured simultaneously without altering the metabolism of the cells. New high-throughput techniques for assessing intratumoral metabolic heterogeneity in large populations of cells are needed to understand the effect of intratumoral heterogeneity on the response of tumours to therapies and to develop new targeted therapies.

With 100% relative sensitivity to optical absorption (that is, a given percentage change in the optical absorption coefficient yields the same percentage change in the photoacoustic amplitude), photoacoustic imaging can provide anatomical, functional, molecular, mechanical and metabolic information about biological tissues[19–23]. Optical-resolution photoacoustic microscopy (OR-PAM), the major microscopic implementation of photoacoustic imaging, achieves diffraction-limited lateral resolution, which is sufficient for single cell imaging[24]. By employing two excitation wavelengths, photoacoustic imaging is the most sensitive technology to measure the oxygen saturation of haemoglobin (sO_2) in blood[25]. Furthermore, by temporally monitoring sO_2, photoacoustic imaging can detect changes in the oxygen content of blood and quantify oxygen metabolism without labelling[26]. Here, we developed single-cell metabolic photoacoustic microscopy (SCM-PAM) by combining a high-density microwell array with wide-field fast-scanning functional OR-PAM. SCM-PAM provides label-free, high-throughput, single-cell OCR measurements for a large population of cells. Each target cell is trapped in a microwell that constitutes a small oxygen-diffusion-limited environment. By using haemoglobin as both an oxygen supplier and sensor, SCM-PAM continuously monitors the sO_2 in each microwell to detect changes in oxygen content and quantify the OCR of each target cell. With the ability to fast-scan over a wide field of view, SCM-PAM can monitor thousands of microwells, thus achieving label-free, high-throughput, single-cell OCR measurements for a large population of cells.

Results

SCM-PAM of single-cell trapping and oxygen sealing in a high-density microwell array. The system schematic of SCM-PAM is shown in Fig. 1a (see Methods). In brief, the laser beams are focused on the high-density microwell array and the generated photoacoustic signals are detected by an ultrasonic transducer. By recording the time course of the photoacoustic signal from each laser pulse, a one-dimensional photoacoustic image (A-line) is acquired. Cross-sectional (B-scans) and volumetric images (C-scans) can be obtained by linear and raster motor scanning, respectively. To provide comprehensive single-cell metabolic information, we operate SCM-PAM in two modes, high-resolution mode and high-throughput mode. In the high-resolution mode (Fig. 1b), the microwell array is placed at the optical and acoustic focal plane of the SCM-PAM. With a scanning step size of 1.25 μm, a photoacoustic image with a field of view of 1 mm × 1 mm (corresponding to 100 microwells) is acquired by SCM-PAM in 400 s. In this mode, we achieve optical-diffraction-limited lateral resolution, which is 2.71 μm for the current system (see Methods and Supplementary Fig. 1). Multiple parameters, including the cell size and the well-filling ratio, can be quantified in the high-resolution mode. In the high-throughput mode (Fig. 1c), the laser beam is slightly defocused so that the laser spot size on the microwell array is 10 μm. A photoacoustic image with a field of view of 7.2 mm × 7.2 mm (corresponding to 3,600 microwells) is then acquired by SCM-PAM with a scanning step size of 20 μm. Each image takes 720 s to acquire in high-throughput mode. In this mode, four spots in each microwell are sampled to provide accurate measurement of sO_2 in the microwell. The throughput can be further improved by sampling only one spot in each microwell at the expense of sO_2-measurement accuracy in the microwell.

We first imaged the high-density microwell array with the SCM-PAM in high-resolution mode. Because the aluminium layer generates strong photoacoustic signals, each microwell can be clearly identified in the photoacoustic images as a negative contrast (Fig. 2a). The microwell diameters estimated from the photoacoustic images were approximately 40 μm, which agreed well with the values set during fabrication. To test the single-cell trapping efficiency of the microwell array, we imaged it loaded
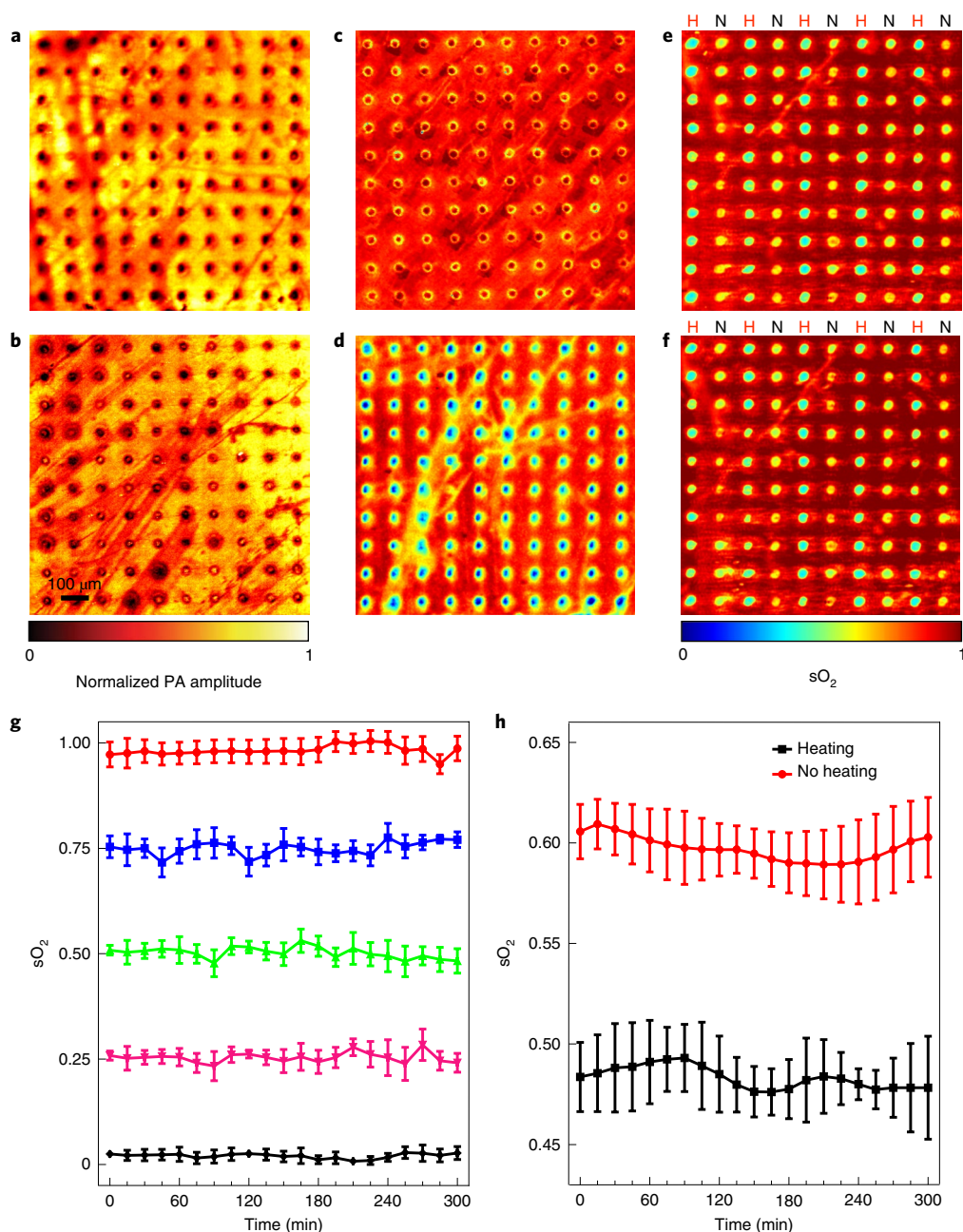
Fig. 2 | SCM-PAM of single-cell trapping and oxygen sealing in a high-density microwell array. a, SCM-PAM of a microwell array without loading. Each well can be clearly identified. **b**, SCM-PAM of a microwell array loaded with a single B16 cell per well. **c**, SCM-PAM of a microwell array loaded with fully oxygenated blood. **d**, SCM-PAM of a microwell array loaded with fully deoxygenated blood. **e**, SCM-PAM of a microwell array loaded with blood immediately after heating select columns. **f**, SCM-PAM of the microwell array loaded with blood 300 min after heating select columns. H, columns with heating; N, columns without heating. **g**, Oxygen sealing of an array from the outside air with various initial sO_2 values. The sO_2 of the blood in the microwells remained unchanged during 300 min of monitoring, showing that the microwell array was fully sealed and there was no oxygen diffusion between the microwells and the outside air ($n=3$ groups; the error bars show the s.d.). **h**, Oxygen sealing of an array between microwells. The sO_2 of the blood in the microwells remained unchanged during 300 min of monitoring after heating select columns, showing that the array was fully sealed and there was no oxygen diffusion between the microwells ($n=3$ groups; the error bars show the s.d.).

with B16 melanoma cells. Individual B16 cells were clearly identified in the microwells (Fig. 2b). By optimizing the cell-trapping procedure, we achieved a cell-trapping efficiency of 73%. We then imaged the microwell array loaded with fully oxygenated blood ($sO_2=100\%$) and fully deoxygenated blood ($sO_2=0\%$). The sO_2 maps of the high-density microwell arrays were obtained by employing two wavelengths (532 and 559 nm) for photoacoustic excitation (Fig. 2c,d). The sO_2 values were measured accurately

and the microwells were clearly distinguished from the background based on the sO_2 values.

To ensure that the OCR for each individual cell was measured accurately, we verified the oxygen sealing of the microwell array. We first studied the oxygen diffusion between the blood in the microwells and the outside air by monitoring the sO_2 in the microwells. The array was loaded with blood with sO_2 values of 0, 25, 50, 75 and 100%, and the sO_2 values in the microwells were
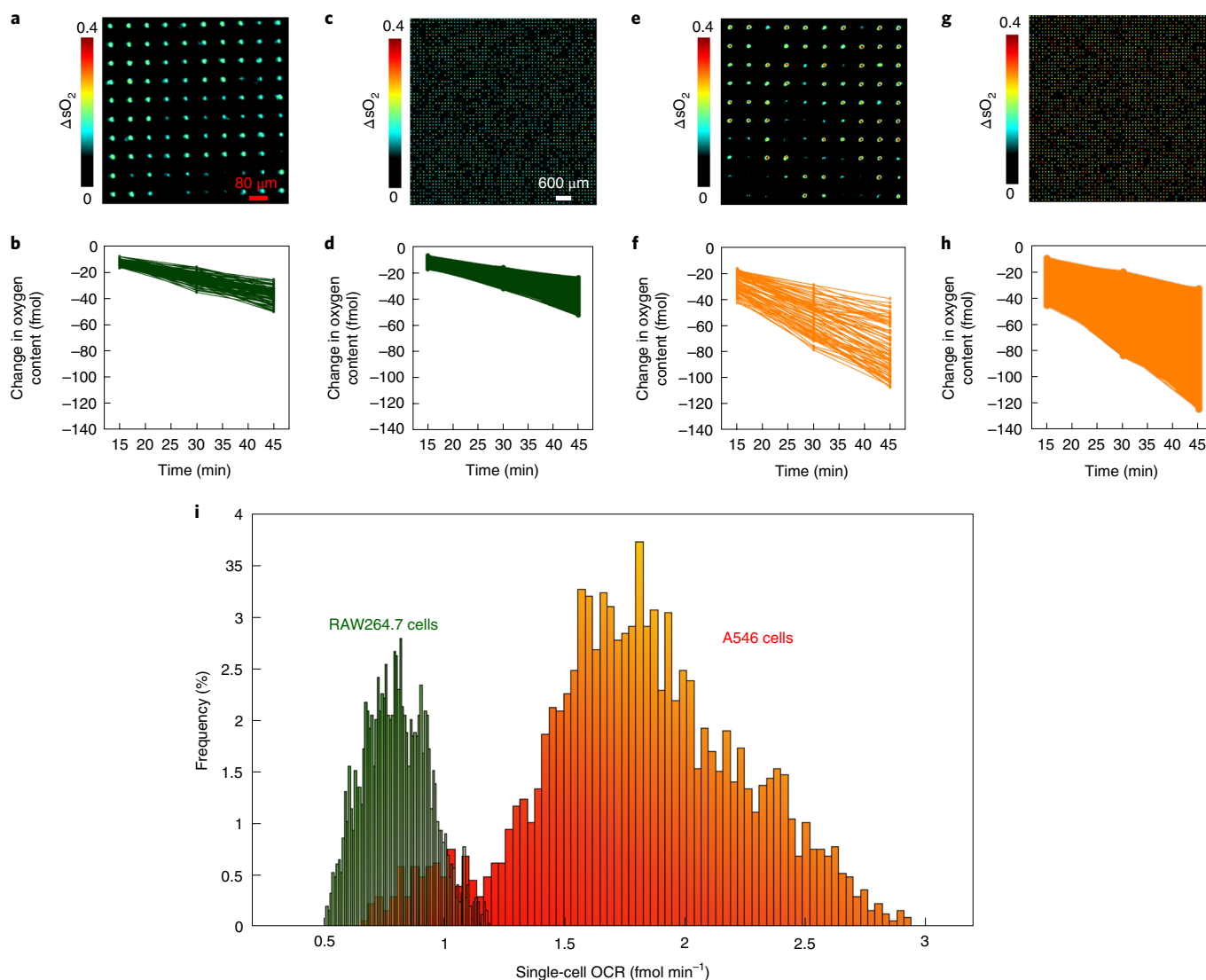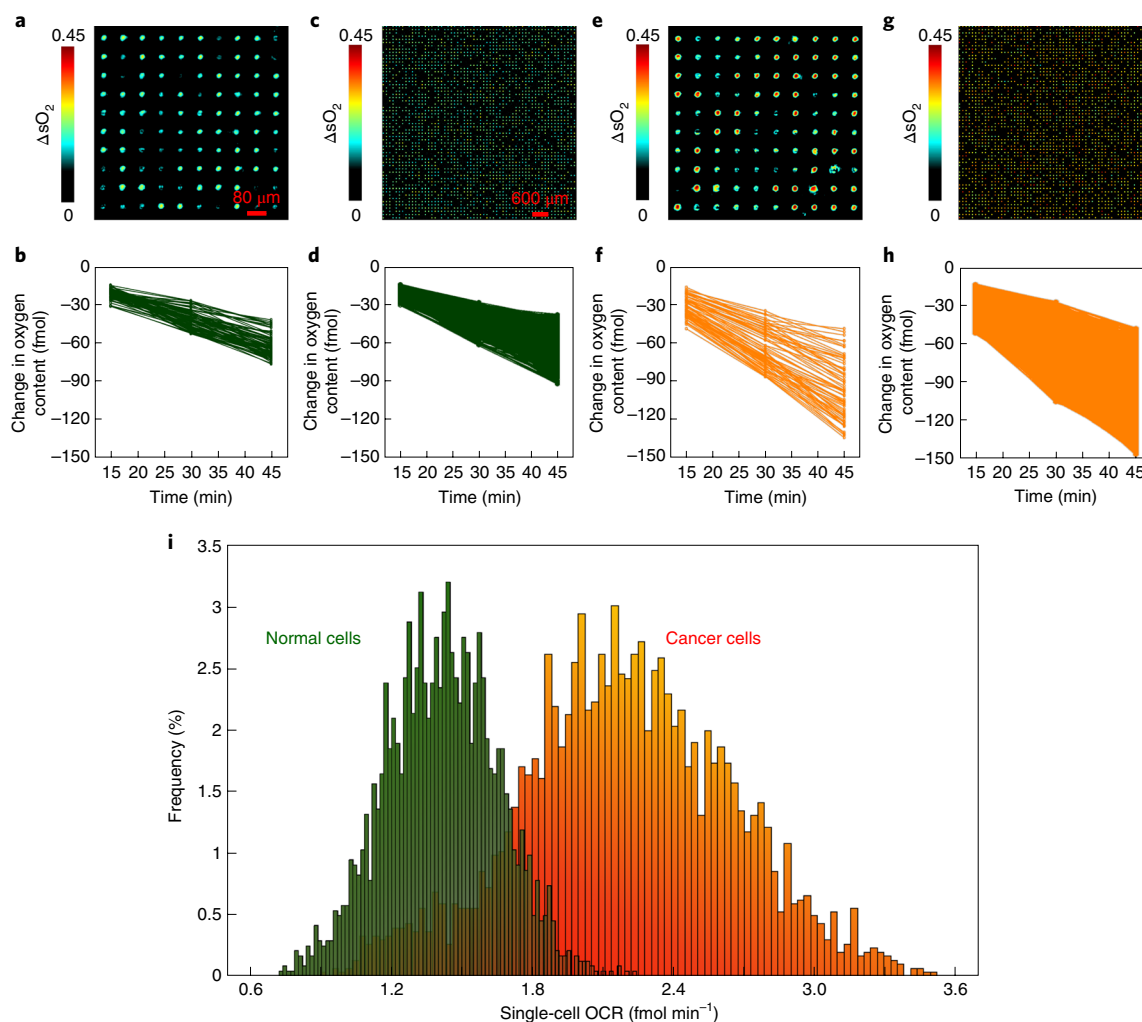
Fig. 3 | SCM-PAM of cellular metabolic heterogeneity in cultured cells. a–d, SCM-PAM of single-cell OCRs of cultured RAW264.7 cells. **a**, SCM-PAM of sO₂ changes in the microwells measured in high-resolution mode. **b**, Oxygen consumption curves of 92 RAW264.7 cells measured by SCM-PAM in high-resolution mode. **c**, SCM-PAM of sO₂ changes in the microwells in high-throughput mode. **d**, Oxygen consumption curves of 2,746 RAW264.7 cells measured by SCM-PAM in high-throughput mode. **e–h**, SCM-PAM of single-cell OCRs of cultured A549 cells. **e**, SCM-PAM of sO₂ changes in the microwells measured in high-resolution mode. **f**, Oxygen consumption curves of 86 A549 cells measured by SCM-PAM in high-resolution mode. **g**, SCM-PAM of sO₂ changes in the microwells in high-throughput mode. **h**, Oxygen consumption curves of 2,761 A549 cells measured by SCM-PAM in high-throughput mode. **i**, Single-cell OCR distribution of the two cell lines, measured by SCM-PAM in high-throughput mode. **b,d,f,h**, Each data point represents the change in oxygen content in a single microwell at a measurement time point. The lines connect the data points at different measurement time points in the same microwell and are guides to allow the visualization of the changes in oxygen content.

monitored for 300 min, which is 20× longer than the 15 min time interval between two sO₂ measurements in later experiments. The sO₂ remained unchanged for 300 min during the imaging (Fig. 2g), showing that the microwells were fully sealed.

To avoid crosstalk between single-cell OCR measurements of adjacent microwells, we then tested for oxygen diffusion between microwells. First, we induced differences in adjacent microwells by selectively heating the microwells, as a change in temperature can shift the oxygen–haemoglobin dissociation curve and thus change the sO₂ in the microwells. The baseline sO₂ of the blood loaded in the array was approximately 60%, the value at which a small shift of the oxygen–haemoglobin dissociation curve can yield a relatively large change in sO₂. Every other microwell column was then heated by scanning a continuous-wave laser (532 nm wavelength) along the

column. During heating, the maximum photoacoustic amplitude increase at 532 nm was about 8.5%, corresponding to a temperature rise of 1.9 °C. To ensure that only the blood in the microwells was heated, the continuous-wave laser spot size was 15 μm and the scanning step size was 80 μm. The laser spot size was smaller than the microwell diameter of 40 μm and the scanning step size matched the spacing between microwells. After heating, the array was sealed immediately with silicone oil and the sO₂ in the microwells was monitored for 300 min (Fig. 2e,f). At the beginning of the monitoring period, an average decrease of 12% in sO₂ was observed, which was due to heating. During the 300 min of monitoring, the sO₂ in microwells with and without heating remained unchanged, demonstrating that there was no oxygen diffusion between the microwells in the high-density microwell array (Fig. 2h).

Fig. 4 | SCM-PAM of intratumoral metabolic heterogeneity in a breast cancer patient. a–d, Single-cell OCRs of normal breast tissue cells measured by SCM-PAM. **a**, SCM-PAM of sO_2 changes in the microwells in high-resolution mode. **b**, Oxygen consumption curves of 87 normal cells measured by SCM-PAM in high-resolution mode. **c**, SCM-PAM of sO_2 changes in the microwells in high-throughput mode. **d**, Oxygen consumption curves of 2,438 normal cells measured by SCM-PAM in high-throughput mode. **e–h**, Single-cell OCRs of cancerous breast tissue cells measured by SCM-PAM. **e**, SCM-PAM of sO_2 changes in the microwells in high-resolution mode. **f**, Oxygen consumption curves of 93 cancer cells measured by SCM-PAM in high-resolution mode. **g**, SCM-PAM of sO_2 changes in the microwells in high-throughput mode. **h**, Oxygen consumption curves of 2,463 cancer cells measured by SCM-PAM in high-throughput mode. **i**, Single-cell OCR distribution of normal and cancer cells from the patient measured, by SCM-PAM in high-throughput mode. **b,d,f,h**, Each data point represents the change in oxygen content in a single microwell at a measurement time point. The lines connect the data points at different measurement time points in the same microwell and are guides to allow the visualization of the change in oxygen content.

SCM-PAM of cellular metabolic heterogeneity in cultured cells.

To validate the basic ability to image cellular metabolic heterogeneity, we first applied SCM-PAM to image cultured normal and cancer cells. Two cell lines, RAW264.7 murine macrophages (a normal cell line) and A549 human epithelial lung cancer cells, were used. The single-cell OCRs of RAW264.7 cells were first measured in high-resolution mode (Fig. 3a). Of 100 microwells, 92 were filled with a single RAW264.7 cell per well. The sO_2 in each microwell was monitored for 45 min to measure the oxygen consumed by individual RAW264.7 cells (see Methods and Fig. 3b). Based on the oxygen consumed in 45 min, the OCR of each cell was calculated. The average single-cell OCR of the 92 RAW264.7 cells was $0.84 \pm 0.08\,fmol\,min^{-1}$. We then switched to high-throughput mode and monitored the sO_2 in 3,600 microwells. Among the 3,600 microwells, 2,746 showed significant changes in sO_2 within the 45 min of monitoring (Fig. 3c), indicating that each of these microwells was loaded with a single living RAW264.7 cell. For the remaining microwells, it could

be that RAW264.7 cells were either not loaded or dead. The oxygen consumed in each microwell was calculated based on the sO_2 change (Fig. 3d) and the single-cell OCRs of the 2,746 RAW264.7 cells were calculated accordingly. The average single-cell OCR of the 2,746 RAW264.7 cells was $0.81 \pm 0.11\,fmol\,min^{-1}$. Similarly, the single-cell OCRs of A549 cells were first measured in high-resolution mode (Fig. 3e). Of 100 microwells, 86 were filled with a single A549 cell. As before, the sO_2 in each microwell was monitored for 45 min and the consumed oxygen was calculated (see Methods and Fig. 3f). The OCR of each cell was then calculated based on the oxygen consumed and the average single-cell OCR of the 86 A549 cells was $1.86 \pm 0.43\,fmol\,min^{-1}$. Among the 3,600 microwells, 2,761 showed significant changes in sO_2 within the 45 min of monitoring in high-throughput mode (Fig. 3g), indicating that a single A549 cell was loaded in each of these wells. The oxygen consumed in each microwell was calculated based on the sO_2 change (Fig. 3h) and the OCRs of the 2,761 A549 cells were calculated accordingly.

The average single-cell OCR was 1.82 ± 0.47 fmol min^{-1}. To show the cellular metabolic heterogeneity, the distributions of the single-cell OCRs of the above two cell lines are shown in a histogram (Fig. 3i). The cancer cell line showed a broader and more irregular distribution of single-cell OCRs, indicating a higher level of cellular metabolic heterogeneity compared with the normal cell line. The initial results in cultured cells demonstrate the ability of SCM-PAM to perform label-free, high-throughput, single-cell OCR measurements and show its potential for imaging intratumoral metabolic heterogeneity.

To fully demonstrate the robustness and specificity of this technique, we applied SCM-PAM to measure the single-cell OCR changes of A549 cells treated with different metabolic inhibitors, including oligomycin (12 μM), an inhibitor of ATP synthase in mitochondria[27], and rotenone (2 μM) and antimycin (2 μM), both inhibitors of the electron transport chain in mitochondria[27]. The single-cell OCR distributions for A549 cells in the presence or absence of the metabolic inhibitors were measured. In all three cases, the metabolic inhibitors significantly decreased the average single-cell OCRs (Supplementary Fig. 3). This pharmacological intervention fully demonstrated the robustness and specificity of SCM-PAM in label-free, high-throughput measurement of single-cell OCRs.

SCM-PAM of intratumoral metabolic heterogeneity in breast cancer patients. To fully demonstrate its potential in imaging intratumoral metabolic heterogeneity, we applied SCM-PAM to measure the single-cell OCR distributions of normal and cancerous breast tissues from three breast cancer patients. After surgical excision, the normal and cancerous breast tissues were dissociated into single-cell suspensions and placed into the device. The single-cell OCRs of normal breast tissue cells from patients were first measured in high-resolution mode (Fig. 4a). Of 100 microwells, 87 were each filled with a single cell. We monitored the sO$_2$ in each microwell for 45 min to quantify the oxygen consumed and calculated the OCR of the cell in the microwell (see Methods and Fig. 4b). The average single-cell OCR of the 87 normal cells was 1.40 ± 0.22 fmol min^{-1}. We then switched to high-throughput mode. Among the 3,600 microwells imaged, 2,438 showed significant changes in sO$_2$ within the 45 min of monitoring (Fig. 4c), indicating that a single cell was loaded in each of these wells. The oxygen consumed in each microwell was calculated based on the sO$_2$ change (Fig. 4d) and the OCR of each single cell was calculated accordingly. The average single-cell OCR of the 2,438 cells from the normal breast tissues was 1.41 ± 0.23 fmol min^{-1}. Similarly, we measured the single-cell OCRs of the breast cancer cells from patients (Fig. 4e–h). In high-resolution mode, the measured average single-cell OCR of 93 single cancer cells was 2.27 ± 0.42 fmol min^{-1}. In high-throughput mode, the measured average single-cell OCR of 2,463 single cancer cells was 2.21 ± 0.45 fmol min^{-1}. To illustrate the cellular metabolic heterogeneity in breast cancer patients, the distributions of single-cell OCRs of the normal and cancer cells were plotted (Fig. 4i and Supplementary Figs. 4,5). Although tumours contain multiple populations of cells beside cancer cells, the cancer specimen had a significantly higher average single-cell OCR, due to its higher rate of metabolism, than those of the normal specimen. Paralleling the results from cultured cells, cells from the cancer tissue also showed a broader and more irregular distribution of single-cell OCRs, indicating a higher degree of cellular metabolic heterogeneity than normal cells. The results from the breast cancer patients fully prove the ability of SCM-PAM to image intratumoral metabolic heterogeneity and show its potential for clinical translation.

Quantification of elevated cellular metabolic heterogeneity in cancer. To show the full capability of SCM-PAM in the quantitative characterization of intratumoral metabolic heterogeneity, we calculated and compared several key parameters of the single-cell OCR distributions of both cultured cells and cells from three breast can-

cer patients. Using cultured cells, we first calculated the coefficients of variation (C_v) of the single-cell OCR distributions of RAW264.7 and A549 cells (see Methods). A549 cells showed a significantly higher C_v than the RAW264.7 cells ($n = 5$ groups, 14,055 RAW264.7 cells and 13,257 A549 cells; $*P = 0.015$), indicating an elevated level of cellular metabolic heterogeneity (Fig. 5a). To quantify how close the single-cell OCR distributions are to normal distributions, we calculated the chi-squared (χ^2) goodness-of-fit to normal distributions for the cultured cells (see Methods). A549 cells had a significantly higher χ^2 value than the RAW264.7 cells ($n = 5$ groups, 14,055 RAW264.7 cells and 13,257 A549 cells; $*P = 0.011$), indicating a lower similarity to normal distributions (Fig. 5b). In other words, there was a higher level of chaotic cellular metabolic heterogeneity in cancer cells than in normal cells.

In subsequent tests using cells from three breast cancer patients, cancer cells had a higher average single-cell OCR, showing an increase in oxygen consumption compared with normal cells (Fig. 5c). We also measured the C_v and χ^2 values of the single-cell OCR distributions of the normal and cancer cells. Cancer cells showed a significantly higher C_v than normal cells ($n = 3$ patients, 7,549 normal cells and 6,807 cancer cells; $*P = 0.013$), indicating an elevated level of cellular metabolic heterogeneity (Fig. 5d). In addition, cancer cells had a significantly higher χ^2 value than normal cells ($n = 3$ patients, 7,549 normal cells and 6,807 cancer cells; $*P = 0.023$), indicating a lower similarity to normal distributions and hence a higher level of chaotic cellular metabolic heterogeneity (Fig. 5e). The quantitative characterization of the intratumoral metabolic heterogeneity further demonstrate the capability of SCM-PAM and its potential as a tool for both preclinical cancer research and clinical cancer therapy.

SCM-PAM of the oxygen consumption of cancer and normal cells in hypoxia. To demonstrate the versatility of SCM-PAM as a research tool, we applied it to study the oxygen consumption of single cells in hypoxia, an important hallmark of cancer. By changing the sO$_2$ of the blood (that is, the oxygen supplier and sensor) in the microwells, we measured how the single-cell OCRs of normal and cancer cells depend on the environmental oxygen levels. In cultured cells, both the A549 and RAW264.7 cells showed decreases in average single-cell OCRs in hypoxia, due to the lower oxygen supply (Fig. 6a). However, A549 cells showed a smaller relative decrease than RAW264.7 cells, indicating better adaptation to hypoxia. We also studied how cellular metabolic heterogeneity changes in hypoxia by measuring the C_v and χ^2 values of single-cell OCR distributions. The C_v values of both RAW264.7 and A549 cells increased in hypoxia, indicating more diverse metabolism of single cells under a lower oxygen supply. A549 cells had an even higher relative change in C_v, demonstrating a greater increase in cellular metabolic heterogeneity (Fig. 6b). The χ^2 values of both RAW264.7 and A549 cells also became larger in hypoxia, showing that the chaotic levels of cellular metabolic heterogeneity increased under a lower oxygen supply (Fig. 6c). An interesting observation is that RAW264.7 cells had a higher relative change in χ^2 values, showing a greater relative increase in the chaotic levels of cellular metabolic heterogeneity. This could be due to two reasons. First, the cancer cells started with a higher baseline level of chaos in cellular metabolic heterogeneity. Second, the cancer cells adapted better to hypoxia than the normal cells, leading to smaller further increases in the chaotic levels of cellular metabolic heterogeneity (Supplementary Fig. 6). Similar results were obtained in cells from the three breast cancer patients (Fig. 6d–f), which further validated the results and show the additional potential of SCM-PAM as an important research tool.

Discussion
By ultrasonically probing the optical absorption of haemoglobin, which acts as both an oxygen supplier and sensor for single cells,
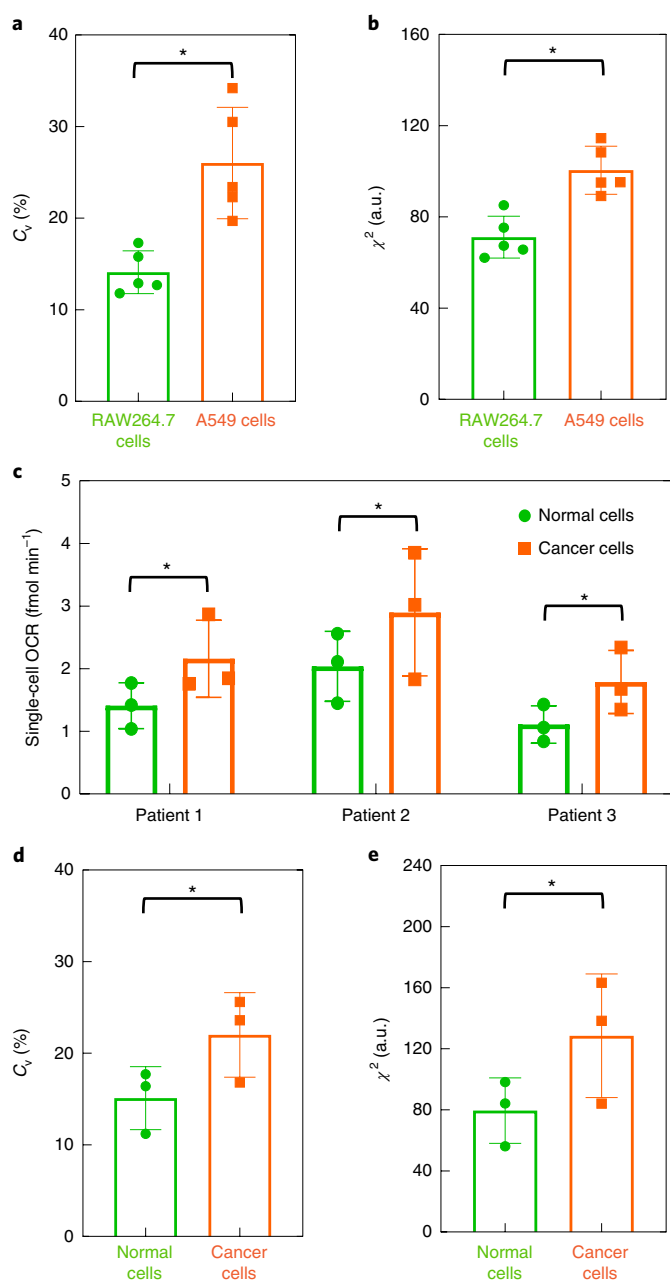
Fig. 5 | Elevated and chaotic cellular metabolic heterogeneity in cancer measured by SCM-PAM. a,b, Elevated cellular metabolic heterogeneity in cultured cells, measured using SCM-PAM ($n = 5$ groups, 14,055 normal cells and 13,257 cancer cells). **a**, C_v values of the single-cell OCR distributions of cultured RAW264.7 and A549 cells. $*P = 0.015$. **b**, Chi-squared goodness-of-fit to normal distributions of the single-cell OCR distributions of RAW264.7 and A549 cells. $*P = 0.011$. **c**, Average single-cell OCRs of normal and cancerous breast tissue cells from three breast cancer patients. For all three patients, the cancer cells consumed oxygen faster than the normal cell on average. $*P = 0.030$, 0.040 and 0.015 for Patients 1, 2 and 3, respectively. **d,e**, Elevated cellular metabolic heterogeneity in breast cancer patients, measured using SCM-PAM ($n = 3$ patients, 7,549 normal cells and 6,807 cancer cells). **d**, C_v values of the single-cell OCR distributions of normal and cancer cells from breast cancer patients. $*P = 0.013$. **e**, Chi-squared goodness-of-fit to normal distributions of the single-cell OCR distributions of normal and cancer cells from breast cancer patients. $*P = 0.023$. Paired one-tailed t-tests were used in the statistical testing; the error bars show the s.d.

photoacoustic imaging achieves label-free OCR measurements. Without the need for exogenous oxygen sensors or labelling, a large population of cells can be screened for single-cell OCR measurement by creating an oxygen-diffusion-limited microenvironment for each cell using a high-density microwell array. Combining photoacoustic imaging with the high-density microwell array, SCM-PAM successfully overcomes all of the major challenges in high-throughput single-cell OCR measurements and enables the imaging of cellular metabolic heterogeneity in cancer. In addition, by mixing cancer cells with whole blood, SCM-PAM avoids possible adverse effects on normal cell functioning that might be caused by embedded oxygen sensors or labelling, oxygen consumption by electrode sensors[28] or photo-toxicity by fluorescent sensors[29]. We initially proved the capability of SCM-PAM in label-free, high-throughput, single-cell OCR measurement by imaging cultured normal and cancer cells. We further showed the full potential of SCM-PAM for clinical translation by imaging the intratumoral metabolic heterogeneity in breast cancer patients. By measuring and comparing the key parameters of single-cell OCR distributions of normal and cancer cells, we demonstrated the capability of SCM-PAM to quantify intratumoral metabolic heterogeneity. In addition, we showed other potential applications of SCM-PAM as a powerful research tool to study the oxygen consumption of single cells in hypoxia. More importantly, we characterized the chaotic feature of intratumoral metabolic heterogeneity with and without hypoxia.

Intratumoral heterogeneity refers to a unique characteristic observed specifically in tumours: cells from the same tumour may exhibit distinct phenotypic or epigenetic states due to mutations acquired during tumour evolution[30]. Heterogeneity can be studied from both genetic and phenotypic perspectives. In this work, we focused on the metabolic phenotype, an important hallmark of cancer. To study intratumoral metabolic heterogeneity, we developed SCM-PAM to measure the single-cell OCR distributions of the cells within the same tumours from breast cancer patients. We also quantitatively analysed the intratumoral metabolic heterogeneity using key parameters such as C_v and χ^2 values. By strict definition, the results obtained by imaging the cultured cells did not reflect intratumoral metabolic heterogeneity as they were not cells from the same tumour. So, the term 'cellular metabolic heterogeneity' was used instead of 'intratumoral metabolic heterogeneity' for the cultured cells. The cultured cells were imaged to validate the ability of SCM-PAM to perform label-free, high-throughput, single-cell OCR measurement and assess the entire spectrum of single-cell OCR distributions.

Only two types of metabolic activities are possible in the microwells containing target cells and blood. One is the metabolism of the target cells, which is the primary interest of this work. The other is the metabolism of red blood cells (RBCs). As oxygen carriers, RBCs do not consume oxygen because they do not have any mitochondria[31]. The changes in oxygen content in the microwells are solely caused by the metabolism of the target cells. Thus, we can accurately measure the single-cell OCRs of the target cells by monitoring the change in oxygen content in the microwells over time.

In the high-resolution mode, each microwell was imaged by SCM-PAM with diffraction-limited lateral resolution. In the high-throughput mode, SCM-PAM sampled four spots, each with a diameter of 10 μm (that is, the laser spot size), in each microwell. The spot diameter was set to 10 μm so that four spots would cover most of the 40-μm-diameter microwell. More importantly, because the measurements were taken 15 min apart in the experiments, the sO_2 value in the microwell should be homogeneous and sampling any region of the microwell should yield similar results.

To account for the cancer cell count in each microwell accurately, we must exclude or minimize two possibilities. The first possibility is that more than one target cell is trapped in a microwell, which is unlikely for the following reason. The microwells are 40 μm in
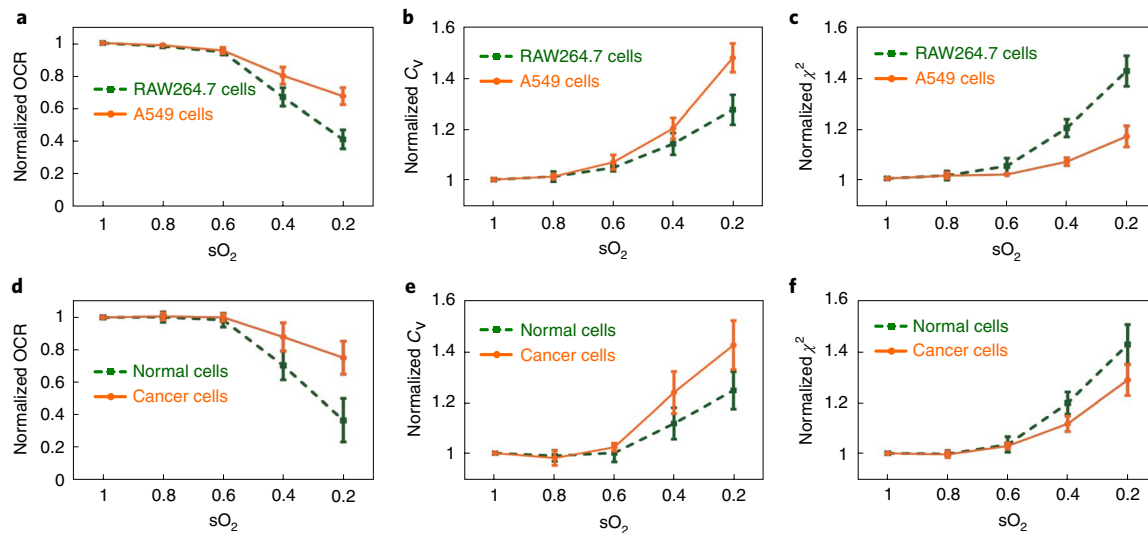
Fig. 6 | Oxygen consumption of cancer and normal cells in hypoxia measured by SCM-PAM. a–c, Oxygen consumption of cultured cells in hypoxia measured by SCM-PAM ($n = 5$ groups). **a**, Normalized single-cell OCRs of cultured RAW264.7 and A549 cells at different sO_2 levels. **b,c**, Normalized C_v (**b**) and χ^2 (**c**) values of the single-cell OCR distributions of RAW264.7 and A549 cells at different sO_2 levels. **d–f**, Oxygen consumption of normal and cancer cells from the three breast cancer patients in hypoxia, measured by SCM-PAM ($n = 3$ patients). **d**, Normalized single-cell OCRs of normal and cancer cells from breast cancer patients at different sO_2 levels. **e,f**, Normalized C_v (**e**) and χ^2 values of the single-cell OCR distributions of normal and cancer cells from breast cancer patients at different sO_2 levels. The error bars show the s.d.

diameter and 50 μm deep, yet the target cells are approximately 15–25 μm in diameter, and they are often irregularly shaped and mixed with a large number of RBCs. The major difficulty in the experiments was to successfully trap a target cell in a microwell and, with careful optimization, we achieved a filling ratio of about 75%. This fill ratio was validated by imaging the high-density microwell array with SCM-PAM in high-resolution mode (Fig. 2b), where no more than one target cell was identified in any microwell. The second possibility is that a microwell is loaded with no cancer cell or with a dead cell. This case was identified and excluded when there was either no or a significantly smaller sO_2 change in a microwell.

There is potential for variability in the total haemoglobin content in each microwell due to different numbers of RBCs in each microwell and to variation in the volumes of target cell. To understand the variability and its effect on the single-cell OCR measurement, we imaged the high-density microwell array loaded with blood or a blood–cell mixture with SCM-PAM in high-resolution mode at an illumination wavelength of 532 nm and quantified the total haemoglobin content over all of the pixels in each microwell. The total variations in haemoglobin content in each microwell were less than 2 and 5% for blood only and the blood–cell mixture, respectively (Supplementary Fig. 7). This small variation is due to the fact that the microwells are much larger than an RBC (diameter of ~3–8 μm and thickness of ~1–2 μm). The variation in measurements of single-cell OCRs was therefore not significant enough to affect the results in the characterization of intratumoral metabolic heterogeneity.

It is worth pointing out that OCR is defined as the volume of oxygen consumed per unit time by a single cell. It represents the overall capability of a single cell to consume oxygen, taking into consideration all other related factors, including cell mass. Thus, we refer to it as single-cell OCR. Elsewhere in the literature, OCR is defined as the volume of oxygen consumed per unit time per unit mass[32]. In this case, OCR essentially reflects the active levels of cellular metabolic pathways or mitochondria in a certain cell type[33]. When OCR is defined in such a way, it is an important parameter to compare cellular metabolism between different cell types. In this work, we aim to study the heterogeneity of metabolic states of single cells from the same tumour—that is, intratumoral metabolic

heterogeneity—with SCM-PAM, instead of comparing cellular metabolism between different cell types. So, the former definition of OCR is used. If SCM-PAM is used to cross compare cellular metabolisms of different cell types, this method is reliable only if the measurements are properly normalized by the cell masses.

Two key parameters, the C_v and χ^2 values, were used in the analysis of intratumoral metabolic heterogeneity. A smaller C_v shows a lower dispersion level in the single-cell OCR distribution. A smaller χ^2 value indicates a lower chaotic level in the single-cell OCR distribution because most cells in the population tend to follow the same normal distribution. A better fit-to-normal distribution does not necessarily indicate a lower dispersion level because the C_v of a single normal distribution can be large. We believe that both the dispersion level (quantified by the C_v) and the chaotic level (quantified by the χ^2 value) are important parameters in describing intratumoral metabolic heterogeneity and hence analysed both aspects.

Both elevated and chaotic metabolic heterogeneity was observed in cancer cells by SCM-PAM in our results. The elevated cellular metabolic heterogeneity can be attributed to the genomic instability in cell cloning and propagation[34], the high potency in cell differentiation—characteristic of cancer stem cells[35]—and the presence of mixed cell populations in the patient specimens. First, cancer-cell propagation results in the constant acquisition of mutations from unstable genome replications, resulting in genomic and phenotypic diversity within a single tumour[36]. Second, cancer stem cells produce a variety of cell types in a tumour through a differentiation hierarchy[37]. Third, tumours are comprised of multiple populations of cells beside the cancer cells themselves, such as inflammatory cells, which may contribute to the metabolic heterogeneity. The genomic diversity, distinct cancer cell types and mixed cell populations within a single tumour result in elevated intratumoral metabolic heterogeneity. Furthermore, the gene expression unpredictability within a single cancer-cell type leads to chaotic cellular metabolic heterogeneity. The high unpredictability of gene expression yields different mitochondrial contents at different times, creating a chaotic metabolic system even in a single cancer cell[38]. Together, these factors contribute to the elevated and chaotic intratumoral metabolic heterogeneity observed by SCM-PAM.

The OCR of an individual cell is the sum of the OCRs of all of the subcellular mitochondria, which are responsible for aerobic glycolysis, that is, oxygen consumption. Mathematically, we have

$$S_n = \sum_{i=1}^{n} M_i \qquad (1)$$

Here, S_n denotes the single-cell OCR, M_i represents the ith mitochondrion OCR and n denotes the virtual number of mitochondria in the cell. Because n is highly consistent[39], it can be treated as a constant within a cell type. According to the central limit theorem, S_n follows a normal distribution if M_i follows the same distribution regardless of its shape. By sampling a massive number of single cells simultaneously, we can accurately model the distributions of S_n and compare them to a normal distribution using the χ^2 test. We found that cancer cells, both in the cultured cell lines as well as the patient tumours, deviated further from normal distributions—that is, with greater χ^2 values—than normal cells, probably due to the aforementioned factors. First, both the genomic diversity and the multiple types of cancer cells within a tumour generate distinct n values and M_i distributions. Second, even within a single cancer cell type, the unpredictability of gene expression produces incongruent distributions of M_i. This observation characterized the chaotic feature of intratumoral metabolic heterogeneity for the first time at the mitochondrial level.

In an effort to further understand the contributions of distinct cancer-cell subclones to intratumoral metabolic heterogeneity, we tried to calculate the number of distinct cell subclones in the sampled cancer cells. By assuming that the single-cell OCR of each cell type follows a normal distribution, we fitted the single-cell OCR distributions of the cancer cells to the sum of multiple normal distributions (Supplementary Fig. 8). The number and weight of the normal distributions were obtained during fitting. The fitting results showed that the distributions of the single-cell OCRs of the cancer cells were the sum of multiple normal distributions, indicating that there may be several cell subclones or types within the cancer cell population examined.

The functionality of SCM-PAM can be further enhanced in two aspects. First, the imaging throughput can be further improved by using an array with more microwells and increasing the imaging speed. To make an array with more microwells, more robust fabrication materials and processes are required. To increase the imaging speed, new scanning mechanisms, such as microelectromechanical system mirror-based scanning, can be used[40]. Second, additional parameters can be measured to provide more information on single-cell metabolism. Cell sizes can be more accurately quantified in three dimensions by using the photobleaching effect[41] and pH values can be measured with a pH-sensitive fluorescent dye[42].

SCM-PAM holds great promise for clinical translation in several areas, including the emerging area of hypoxia targeting, understanding metabolic diversity within and between tumours, and investigating the effect of the metabolic heterogeneity on tumour phenotype and drug responsiveness. First, SCM-PAM only requires tumour dissociation into a single-cell suspension with no further special sample preparation required, which makes it easy and convenient for clinical adoption. Second, it takes less than 20 min for SCM-PAM to obtain the single-cell OCR distribution of one patient, which is sufficiently short for clinical application. Third, although in this work we have focused on breast cancer, SCM-PAM can be applied to image intratumoral metabolic heterogeneity of virtually all solid tumours that can be sampled. The microwell size can be adjusted to better accommodate different cancer cells of varying size. Fourth, there is the potential for cell retrieval from the device so that molecular analysis can be performed on individual cells to correlate with their intrinsic metabolic activity or to assess their biological phenotype.

The information obtained on single-cell metabolism and intratumoral metabolic heterogeneity will be particularly valuable to cancer therapy[43]. Information on the single-cell metabolism of cancer cells can be used for therapy response monitoring and evaluation[44], which can help screen drug combinations and develop personalized cancer therapy strategies[45]. For example, the metabolic heterogeneity can be assessed in residual tumours after neoadjuvant treatment to determine whether specific metabolically active cell populations are resistant or sensitive to therapy. Apart from cancer therapy, by measuring the single-cell OCR distributions of different tumours in one patient, SCM-PAM can also be used to investigate intertumoural heterogeneity and response to therapy. Moreover, SCM-PAM is particularly suitable for studying the metabolic states of circulating tumour cells, the key determinants of cancer metastatic propensity, because blood is the original biological environment for circulating tumour cells[46].

In summary, we have developed and optimized SCM-PAM, which combines a wide-field fast-scanning functional OR-PAM with a high-density microwell array, for the label-free, high-throughput, single-cell imaging of intratumoral metabolic heterogeneity. We have demonstrated its capability by measuring the single-cell OCR distributions of cultured cells and showed its potential for clinical translation by imaging intratumoral metabolic heterogeneity in patient breast cancer specimens. In addition, with rich optical absorption contrast, the wide-field fast-scanning functional OR-PAM subsystem of SCM-PAM may provide specific insights into angiogenic potential, metastatic propensity and drug sensitivity—all on a cellular level—as well as intratumoral heterogeneity[47–49]. With its unique capability for label-free, high-throughput, single-cell OCR measurements and the potential to provide multidimensional information about tumours, SCM-PAM is a promising tool for both fundamental cancer research and personalized clinical cancer therapy.

Methods

SCM-PAM system. To achieve label-free, high-throughput, single-cell metabolic imaging, we combined a functional OR-PAM system with a high-density microwell array (Fig. 1). For sO$_2$ measurement, the system employs a solid-state laser at 532 nm (SPOT, Elforlight) and a dye laser (CBR-D, Sirah) at 559 nm. The combined laser beam was reshaped by a 2 mm aperture iris (ID25SS, Thorlabs) and attenuated by a neutral density filter (NDC-50C-2M, Thorlabs). A pair of condenser lenses (LA1131, Thorlabs) and a pinhole (P50C, Thorlabs; diameter of 50 μm) were used to spatially filter the laser beam. A beam sampler (BSF10-A, Thorlabs) and a photodiode were used to monitor the laser intensity fluctuation. The filtered laser beam was then coupled to a single-mode photonic crystal fibre (LMA-10, NKT Photonics). The output of the single-mode fibre was collimated by an objective lens (RMS4X, Thorlabs), reflected by a mirror and focused on the object by another identical objective lens. A beam combiner, composed of a thin layer of silicone oil sandwiched by a rhomboid prism (NT49-419, Edmund Optics) and a right-angle prism (NT32-545, Edmund Optics), provided acoustic–optical coaxial alignment. The generated photoacoustic waves were detected by an ultrasonic transducer with a central frequency of 50 MHz (V214-BB-RM, Olympus-NDT) placed confocally with the objective lens.

Lateral resolution of SCM-PAM. The lateral resolution of the SCM-PAM system was measured by imaging a sharp metal edge with a scanning step size of 0.625 μm and a scanning range of 100 μm along the x axis (Supplementary Fig. 1). The measured data were fitted to an edge spread function and the line spread function was calculated based on the fitted edge spread function. The full width at half maximum of the line spread function was quantified as the lateral resolution. The experimentally measured lateral resolution of SCM-PAM was 2.71 μm, which is close to the theoretical value of 2.66 μm.

High-density microwell array. To achieve label-free, high-throughput, single-cell metabolic imaging, we designed and fabricated a high-density microwell array capable of trapping a single cell in each microwell. To ensure that no more than one cell was trapped, each microwell was designed with a diameter of 40 μm and depth of 50 μm, and the microwells were set 80 μm apart. SU-8 50 (NANO) resist was used for fabrication of the microwell array. To enable the effective loading of cells and blood without trapping air in the microwells, the array was fabricated on an anodisc inorganic filter membrane (Whatman). To improve adhesion between the SU-8 substrate and the anodisc inorganic filter membrane, a 400-nm-thick layer of aluminium was deposited between them. The anodisc inorganic filter membrane

did not function as an oxygen reservoir. The experiments used whole blood with intact RBCs. Because RBCs are approximately 3–8 μm in diameter and the pore size of the filter membrane was 100 nm, only plasma, in which dissolved oxygen is negligible, could pass through the filter membrane. Hence, the filter membrane did not increase the oxygen capacity of the microwells and it had a negligible effect on the calculation of single-cell OCR. In addition, the pores in the filter membrane are not connected with each other, so oxygen cannot diffuse between microwells.

The detailed fabrication process was as follows (Supplementary Fig. 2). First, a 400-nm-thick layer of aluminium was deposited on one side of a 60-μm-thick anodisc inorganic filter membrane by an e-beam evaporator (Kurt J. Lesker). Second, SU-8 50 was spin coated on the aluminium layer at 500 r.p.m. for 10 s in the spread cycle and at 4,000 r.p.m. for 30 s in the spin cycle to generate a 50-μm-thick layer of SU-8 substrate. The entire substrate was then soft baked in an oven at 90 °C for 3 h, after which the SU-8 was exposed to near-ultraviolet light at 200 mJ cm⁻². After post-exposure baking, the microwells were developed in an SU-8 developer. The entire high-density microwell array was then immersed in aluminium etchant, during which the aluminium layer beneath the microwells was etched away, while the remaining part of the aluminium layer was kept.

Cell culture and reagents. Three types of cells (B16 mouse melanoma, RAW264.7 and A549 cell lines) were obtained from the Tissue Culture and Support Centre at the Washington University School of Medicine. The B16 and RAW264.7 cells were cultured in Dulbecco's Modified Eagle medium (Invitrogen) supplemented with 10% fetal bovine serum (Invitrogen) at 37 °C in 5% CO_2. The A549 cells were cultured in F-12K medium at 37 °C in 5% CO_2. At 75–80% confluence, the cells were harvested with 0.25% trypsin–EDTA solution (Invitrogen) to generate a single-cell suspension at a concentration of 1×10^6 cells ml⁻¹ and then mixed with the same volume of blood (cat. no. 910, Quad Five). In the pharmacological intervention experiments, 12 μM oligomycin (AB143424, Abcam), 2 μM rotenone (cat. no. 45656, Sigma-Aldrich) and 2 μM antimycin (A8674, Sigma-Aldrich) were added to the blood-cell mixture.

Cells from patient specimens. After informed consent was obtained, breast cancer and normal tissues were collected from women with newly diagnosed clinical stage I/II breast cancer undergoing breast-conserving surgery. The cancer tissues primarily consisted of cancer cells and may also have contained some stromal cells. The normal tissues were from the same breasts, but distant from the cancer. They were primarily adipose tissue and may have contained fibrous breast tissue. The protocol was approved by the Institutional Review Board at the Washington University in St. Louis. After excision, the breast tissue was immediately transported in saline from the operating room to the lab and dissociated to a single-cell suspension with a gentleMACS Dissociator (Miltenyi Biotec) with minimal ischaemia time.

Label-free, high-throughput, single-cell OCR measurement by SCM-PAM. To achieve label-free, high-throughput, single-cell OCR measurement, 0.1 ml of the single-cell suspension containing ~10,000 single cells was mixed with the same volume of fully oxygenated blood (cat. no. 910, Quad Five) and loaded into the high-density microwell array. After waiting for the cells to settle into the microwells, the high-density microwell array was gently flushed with fully oxygenated blood and fresh cell culture medium to remove cells outside the microwells and a small rubber squeegee was subsequently drawn across the flat surface. After gently immersing the microwell array in silicone oil for oxygen sealing, the entire assembly was transferred to SCM-PAM for single-cell OCR measurement. During the single-cell OCR measurement, a lab-made heating pad maintained the temperature.

Because the amount of oxygen dissolved in blood is negligible compared with its counterpart bound to haemoglobin, the sO_2 change in a microwell can be considered reflective of the change in oxygen content in the microwell. The OCR of a single cell in a microwell can be calculated by:

$$OCR = \frac{\Delta O_2}{\Delta t} \qquad (2)$$

Here ΔO_2 represents the amount of oxygen change in the microwell over a certain time period Δt. The oxygen change in a microwell can be calculated by:

$$\Delta n = V_b \times \Delta C_{bO_2} \qquad (3)$$

Where V_b is the volume of blood in the microwell, which is 4.9×10^4 fl and ΔC_{bO_2} is the change of oxygen concentration in the blood, which is proportional to the sO_2 change ΔsO_2:

$$\Delta C_{bO_2} = 4 \times \Delta sO_2 \times C_{Hb} \qquad (4)$$

Here C_{Hb} is the concentration of haemoglobin in the blood and the factor 4 is the bonding ratio between oxygen and haemoglobin. Combining the above three equations, the OCR can be calculated by:

$$OCR = \frac{4 \times V_b \times \Delta sO_2 \times C_{Hb}}{\Delta t} \qquad (5)$$

Single-cell OCR measurement in hypoxia. To evaluate the OCRs of single cells in hypoxia, blood with sO_2 of 100, 80, 60, 40 and 20% were used in the experiments. They were obtained by mixing fully oxygenated blood with fully deoxygenated blood at the appropriate ratios. For example, the blood with 80% sO_2 was obtained by mixing fully oxygenated blood with fully deoxygenated blood at a ratio of 4:1. Similarly, the ratios used to obtain blood with 60, 40 and 20% sO_2 were 3:2, 2:3 and 1:4, respectively.

C_v and χ^2 goodness-of-fit. The coefficient of variation C_v is defined as the ratio of the standard deviation σ to the mean μ of a distribution:

$$C_v = \frac{\sigma}{\mu} \qquad (6)$$

It is a normalized measure of the dispersion of the single-cell OCR distribution and thus a parameter to quantify and compare intratumoral metabolic heterogeneity.

The χ^2 goodness-of-fit was used to assess how close the single-cell OCR distribution was to a normal distribution. The data was first grouped into bins, and the observed and expected counts for the bins were next calculated. The χ^2 value was then calculated by

$$\chi^2 = \sum_{i=1}^{N} \frac{(O_i - E_i)^2}{E_i}. \qquad (7)$$

Here O_i denotes the observed counts and E_i denotes the expected counts based on the normal distribution. A smaller χ^2 value indicates a better fit to the normal distribution and a lower level of intratumoral cellular metabolic heterogeneity.

Reporting Summary. Further information on research design is available in the Nature Research Reporting Summary linked to this article.

Data availability
The authors declare that all data supporting the results in this study are available within the paper and its Supplementary information. The source data for the figures in this study are available in (identifier figshare)[50].

References
1. Fisher, R., Pusztai, L. & Swanton, C. Cancer heterogeneity: implications for targeted therapeutics. *Br. J. Cancer* **108**, 479–485 (2013).
2. Almendro, V., Marusyk, A. & Polyak, K. Cellular heterogeneity and molecular evolution in cancer. *Annu. Rev. Pathol.* **8**, 277–302 (2013).
3. Zhao, Y., Butler, E. B. & Tan, M. Targeting cellular metabolism to improve cancer therapeutics. *Cell Death Dis.* **4**, e532 (2013).
4. Robertson-Tessi, M., Gillies, R. J., Gatenby, R. A. & Anderson, A. R. A. Impact of metabolic heterogeneity on tumor growth, invasion, and treatment outcomes. *Cancer Res.* **75**, 1567–1579 (2015).
5. Patel, A. P. et al. Single-cell RNA-seq highlights intratumoral heterogeneity in primary glioblastoma. *Science.* **344**, 1396–1401 (2014).
6. Sengupta, D. & Pratx, G. Imaging metabolic heterogeneity in cancer. *Mol. Cancer* **15**, 4 (2016).
7. Hensley, C. T. et al. Metabolic heterogeneity in human lung tumors. *Cell* **164**, 681–694 (2016).
8. Grimes, D. R., Warren, D. R. & Warren, S. Hypoxia imaging and radiotherapy: bridging the resolution gap. *Br. J. Radiology* **90**, 20160939 (2017).
9. Xu, H. N., Zheng, G., Tchou, J., Nioka, S. & Li, L. Z. Characterizing the metabolic heterogeneity in human breast cancer xenografts by 3D high resolution fluorescence imaging. *+* **2**, 73 (2013).
10. Georgakoudi, I. & Quinn, K. P. Optical imaging using endogenous contrast to assess metabolic state. *Annu. Rev. Biomed. Eng.* **14**, 351–367 (2012).
11. Alhallak, K., Rebello, L. G., Muldoon, T. J., Quinn, K. P. & Rajaram, N. Optical redox ratio identifies metastatic potential-dependent changes in breast cancer cell metabolism. *Biomed. Opt. Express* **7**, 4364–4374 (2016).
12. Hou, J. et al. Correlating two-photon excited fluorescence imaging of breast cancer cellular redox state with seahorse flux analysis of normalized cellular oxygen consumption. *J. Biomed. Opt.* **21**, 060503 (2016).
13. Wagner, B. A., Venkataraman, S. & Buettner, G. R. The rate of oxygen utilization by cells. *Free Radic. Biol. Med.* **51**, 700–712 (2011).
14. Ferrick, D. A., Neilson, A. & Beeson, C. Advances in measuring cellular bioenergetics using extracellular flux. *Drug Discov. Today* **13**, 268–274 (2008).
15. Molter, T. W. et al. A microwell array device capable of measuring single-cell oxygen consumption rates. *Sens. Actuators B* **135**, 678–686 (2009).
16. Osbourn, D. M., Sanger, R. H. & Smith, P. J. S. Determination of single-cell oxygen consumption with impedance feedback for control of sample-probe separation. *Anal. Chem.* **77**, 6999–7004 (2005).

17. Kuang, Y. & Walt, D. R. Detecting oxygen consumption in the proximity of *Saccharomyces cerevisiae* cells using self-assembled fluorescent nanosensors. *Biotechnol. Bioeng.* **96**, 318–325 (2007).
18. Etzkorn, J. R. et al. Using micro-patterned sensors and cell self-assembly for measuring the oxygen consumption rate of single cells. *J. Micromech. Microeng.* **20**, 095017 (2010).
19. Wang, L. V. & Yao, J. A practical guide to photoacoustic tomography in the life sciences. *Nat. Methods* **13**, 627–638 (2016).
20. Guggenheim, J. A. et al. Ultrasensitive plano-concave optical microresonators for ultrasound sensing. *Nat. Photonics* **11**, 714–719 (2017).
21. Yang, J. et al. Motionless volumetric photoacoustic microscopy with spatially invariant resolution. *Nat. Commun.* **8**, 780 (2017).
22. Wong, T. T. W. et al. Fast label-free multilayered histology-like imaging of human breast cancer by photoacoustic microscopy. *Sci. Adv.* **3**, e1602168 (2017).
23. Hai, P., Zhou, Y., Liang, J., Li, C. & Wang, L. V. Photoacoustic tomography of vascular compliance in humans. *J. Biomed. Opt.* **20**, 126008 (2015).
24. Hai, P., Yao, J., Maslov, K. I., Zhou, Y. & Wang, L. V. Near-infrared optical-resolution photoacoustic microscopy. *Opt. Lett.* **39**, 5192–5195 (2014).
25. Hu, S., Maslov, K. & Wang, L. V. Second-generation optical-resolution photoacoustic microscopy with improved sensitivity and speed. *Opt. Lett.* **36**, 1134–1136 (2011).
26. Yao, J., Maslov, K. I., Zhang, Y., Xia, Y. & Wang, L. V. Label-free oxygen-metabolic photoacoustic microscopy in vivo. *J. Biomed. Opt.* **16**, 076003 (2011).
27. Yang, M., Chadwick, A. E., Dart, C., Kamishima, T. & Quayle, J. M. Bioenergetic profile of human coronary artery smooth muscle cells and effect of metabolic intervention. *PLoS ONE* **12**, 0177951 (2017).
28. Swartz, H. M. Measuring real levels of oxygen in vivo: opportunities and challenges. *Biochem. Soc. Trans.* **30**, 248–252 (2002).
29. Wilson, D. F. et al. Oxygen distribution and vascular injury in the mouse eye measured by phosphorescence-lifetime imaging. *Appl. Opt.* **44**, 5239–5248 (2005).
30. Yap, T. A. et al. Intratumor heterogeneity: seeing the wood for the trees. *Sci. Transl. Med.* **4**, 127ps110 (2012).
31. Berg, C. P. et al. Human mature red blood cells express caspase-3 and caspase-8, but are devoid of mitochondrial regulators of apoptosis. *Cell Death Differ.* **8**, 1197–1206 (2001).
32. Grimes, D. R., Kelly, C., Bloch, K. & Partridge, M. A method for estimating the oxygen consumption rate in multicellular tumour spheroids. *J. R. Soc. Interface* **11**, 20131124 (2014).
33. Thomlinson, R. H. & Gray, L. H. The histological structure of some human lung cancers and the possible implications for radiotherapy. *Br. J. Cancer* **9**, 539–549 (1955).
34. Campbell, P. J. et al. The patterns and dynamics of genomic instability in metastatic pancreatic cancer. *Nature* **467**, 1109–1113 (2010).
35. Clevers, H. The cancer stem cell: premises, promises and challenges. *Nat. Med.* **17**, 313–319 (2011).
36. McGranahan, N. & Swanton, C. Clonal heterogeneity and tumor evolution: past, present, and the future. *Cell* **168**, 613–628 (2017).
37. Meacham, C. E. & Morrison, S. J. Tumour heterogeneity and cancer cell plasticity. *Nature* **501**, 328–337 (2013).
38. Gupta, P. B. et al. Stochastic state transitions give rise to phenotypic equilibrium in populations of cancer cells. *Cell* **146**, 633–644 (2011).
39. Robin, E. D. & Wong, R. Mitochondrial DNA molecules and virtual number of mitochondria per cell in mammalian cells. *J. Cell. Physiol.* **136**, 507–513 (1988).
40. Yao, J. et al. High-speed label-free functional photoacoustic microscopy of mouse brain in action. *Nat. Methods* **12**, 407–410 (2015).
41. Yao, J., Wang, L., Li, C., Zhang, C. & Wang, L. V. Photoimprint photoacoustic microscopy for three-dimensional label-free subdiffraction imaging. *Phys. Rev. Lett.* **112**, 014302 (2014).
42. Chatni, M. R. et al. Functional photoacoustic microscopy of pH. *J. Biomed. Opt.* **16**, 100503 (2011).
43. Galluzzi, L., Kepp, O., Vander Heiden, M. G. & Kroemer, G. Metabolic targets for cancer therapy. *Nat. Rev. Drug Discov.* **12**, 829–846 (2013).
44. Weinberg, S. E. & Chandel, N. S. Targeting mitochondria metabolism for cancer therapy. *Nat. Chem. Biol.* **11**, 9–15 (2014).
45. Wong, A. H.-H. et al. Drug screening of cancer cell lines and human primary tumors using droplet microfluidics. *Sci. Rep.* **7**, 9109 (2017).
46. Hai, P. et al. Label-free high-throughput detection and quantification of circulating melanoma tumor cell clusters by linear-array-based photoacoustic tomography. *J. Biomed. Opt.* **22**, 41004 (2016).
47. Lin, R. et al. Longitudinal label-free optical-resolution photoacoustic microscopy of tumor angiogenesis in vivo. *Quant. Imaging Med. Surg.* **5**, 23–29 (2015).
48. Luke, G. P. & Emelianov, S. Y. Label-free detection of lymph node metastases with US-guided functional photoacoustic imaging. *Radiology* **277**, 435–442 (2015).
49. Cash, K. J., Li, C., Xia, J., Wang, L. V. & Clark, H. A. Optical drug monitoring: photoacoustic imaging of nanosensors to monitor therapeutic lithium in vivo. *ACS Nano* **9**, 1692–1698 (2015).
50. Hai, P. et al. Dataset for high-throughput label-free single-cell photoacoustic microscopy of intratumoral metabolic heterogeneity. *Figshare* https://doi.org/10.6084/m9.figshare.7744004 (2019).

Author contributions

P.H., J.Z. and L.V.W. conceived and designed the study. P.H. and T.I. developed the photoacoustic imaging system. S.X. fabricated the high-density microwell array. R.Z. cultured the cells. R.L.A. provided the excised breast cancer and normal tissues. P.H. and T.I. performed the experiments. P.H. and T.I. analysed the data. L.V.W. supervised the study. All authors wrote the manuscript.

Competing interests

L.V.W. has a financial interest in Microphotoacoustics, Inc.; CalPACT, LLC and Union Photoacoustic Technologies, Ltd. These companies did not support this work.

Additional information

Supplementary information is available for this paper at https://doi.org/10.1038/s41551-019-0376-5.

Reprints and permissions information is available at www.nature.com/reprints.

Correspondence and requests for materials should be addressed to J.Z. or L.V.W.

Publisher's note: Springer Nature remains neutral with regard to jurisdictional claims in published maps and institutional affiliations.

nature research

Corresponding author(s): Lihong V. Wang

Last updated by author(s): Feb 24, 2019

Reporting Summary

Nature Research wishes to improve the reproducibility of the work that we publish. This form provides structure for consistency and transparency in reporting. For further information on Nature Research policies, see Authors & Referees and the Editorial Policy Checklist.

Statistics

For all statistical analyses, confirm that the following items are present in the figure legend, table legend, main text, or Methods section.

n/a	Confirmed	
☐	☒	The exact sample size (*n*) for each experimental group/condition, given as a discrete number and unit of measurement
☐	☒	A statement on whether measurements were taken from distinct samples or whether the same sample was measured repeatedly
☐	☒	The statistical test(s) used AND whether they are one- or two-sided *Only common tests should be described solely by name; describe more complex techniques in the Methods section.*
☐	☒	A description of all covariates tested
☐	☒	A description of any assumptions or corrections, such as tests of normality and adjustment for multiple comparisons
☐	☒	A full description of the statistical parameters including central tendency (e.g. means) or other basic estimates (e.g. regression coefficient) AND variation (e.g. standard deviation) or associated estimates of uncertainty (e.g. confidence intervals)
☐	☒	For null hypothesis testing, the test statistic (e.g. *F*, *t*, *r*) with confidence intervals, effect sizes, degrees of freedom and *P* value noted *Give P values as exact values whenever suitable.*
☒	☐	For Bayesian analysis, information on the choice of priors and Markov chain Monte Carlo settings
☒	☐	For hierarchical and complex designs, identification of the appropriate level for tests and full reporting of outcomes
☒	☐	Estimates of effect sizes (e.g. Cohen's *d*, Pearson's *r*), indicating how they were calculated

Our web collection on statistics for biologists contains articles on many of the points above.

Software and code

Policy information about availability of computer code

Data collection	LabVIEW 2013 and MATLAB R2016b.
Data analysis	MATLAB R2016b and Graphpad Prism 7.

For manuscripts utilizing custom algorithms or software that are central to the research but not yet described in published literature, software must be made available to editors/reviewers. We strongly encourage code deposition in a community repository (e.g. GitHub). See the Nature Research guidelines for submitting code & software for further information.

Data

Policy information about availability of data

All manuscripts must include a data availability statement. This statement should provide the following information, where applicable:

- Accession codes, unique identifiers, or web links for publicly available datasets
- A list of figures that have associated raw data
- A description of any restrictions on data availability

The authors declare that all data supporting the results in this study are available within the paper and its Supplementary Information. Source data for the figures in this study are available in figshare with the identifier doi:10.6084/m9.figshare.7744004.

Field-specific reporting

Please select the one below that is the best fit for your research. If you are not sure, read the appropriate sections before making your selection.

☒ Life sciences   ☐ Behavioural & social sciences   ☐ Ecological, evolutionary & environmental sciences

Life sciences study design

All studies must disclose on these points even when the disclosure is negative.

Sample size	Standard size was chosen. Data were analyzed by using 5 groups of biological replicates (cultured cell lines) and 3 independent experiments (patients' specimens). The sample size n is stated in each figure caption.
Data exclusions	No data were excluded.
Replication	Every experiment of OCR measurement on cultured cell lines was repeated on 5 groups of single cells. The experiment of single-cell OCR measurement on patients' specimens was repeated on 3 patients.
Randomization	The samples were not randomized. The biological samples were included to demonstrate the unique capabilities of SCM-PAM rather than for specific and comprehensive biological studies.
Blinding	Investigators were not blinded to group allocation.

Reporting for specific materials, systems and methods

We require information from authors about some types of materials, experimental systems and methods used in many studies. Here, indicate whether each material, system or method listed is relevant to your study. If you are not sure if a list item applies to your research, read the appropriate section before selecting a response.

Materials & experimental systems

n/a	Involved in the study
☒	☐ Antibodies
☐	☒ Eukaryotic cell lines
☒	☐ Palaeontology
☒	☐ Animals and other organisms
☐	☒ Human research participants
☒	☐ Clinical data

Methods

n/a	Involved in the study
☒	☐ ChIP-seq
☒	☐ Flow cytometry
☒	☐ MRI-based neuroimaging

Eukaryotic cell lines

Policy information about cell lines

Cell line source(s)	The B16 mouse melanoma cell line, the RAW264.7 murine macrophage cell line, and the A549 human epithelial lung cancer cell line were obtained from the Tissue Culture and Support Center at the Washington University School of Medicine.
Authentication	All the cell lines used were authenticated by the Tissue Culture and Support Center at the Washington University School of Medicine before distribution to us.
Mycoplasma contamination	All the cell lines were tested for mycoplasma contamination at the Tissue Culture and Support Center at the Washington University School of Medicine.
Commonly misidentified lines (See ICLAC register)	No commonly misidentified cell lines were used.

Human research participants

Policy information about studies involving human research participants

Population characteristics	The age range of the patients were 34 to 59 years old.
Recruitment	Patients with newly diagnosed clinical stage I/II breast cancer undergoing breast-conserving surgery. If informed consent was obtained from the patient, breast cancer and normal tissues were collected. There was no potential self-selection bias or other biases.
Ethics oversight	The protocol was approved by the Institutional Review Board at Washington University in St. Louis.

Note that full information on the approval of the study protocol must also be provided in the manuscript.